Impact of thermal loads on interfacial debonding in FRP strengthened beams

Oded Rabinovitch *,1

Faculty of Civil and Environmental Engineering, Technion – Israel Institute of Technology, Technion City, Haifa 32000, Israel

ARTICLE INFO

ABSTRACT

The effect of thermal loads on the debonding mechanisms in beams strengthened with externally bonded composite materials is analytically investigated. The analytical approach adopts a high-order stress analysis model and a fracture mechanics model that uses the concept of the energy release rate through the thermo-mechanical form of the *J*-integral. The two models are combined to synthesize the relation between the energy release rate, the mechanical loads, the thermal loads, and the interfacial crack length simulating the thermo-mechanical debonding process. The model is supported through comparison with experimental results taken from the literature. The comparison quantifies and explains various phenomena observed in the experiments and mainly the non-monotonic dependency of the debonding failure load on the temperature. The impact of the temperature on the interfacial stresses and on the stability of the debonding process is also studied. Finally, the effect of an uniform thermal load on the debonding behavior of a strengthened beam is studied revealing the impact of the thermal load on the debonding stability and strength characteristics.

1. Introduction

The strengthening of structural elements with bonded fiber reinforced polymers (FRP) is now an accepted upgrade technique. Along with its vast advantages, this strengthening technique is associated with unique and, in most cases, problematic failure modes. The debonding failure mode, in which the external layer peels off from the concrete substrate, is probably the most critical one. This mode of failure is usually triggered by the stress concentration near irregular point such as crack, unbonded areas, or ends of the composite layer. Then, it propagates as an interfacial crack or few millimeters within the concrete substrate. In both cases, significant parts of the debonding process (if not all of it) are unstable with a rapid crack growth and a brittle failure.

The strengthened beam combines the concrete element, the adhesive layer, and the composite reinforcement. These components significantly differ in their geometrical, mechanical, and elastic properties. On top of that, they differ in their coefficients of thermal expansion (CTEs), see ACI 440 (2002). The CTE mismatch and the inevitable exposure to thermal loads result in strain differentials and thermally induced stresses. These stresses tend to concentrate near irregular points such as cracks, debonded regions, or edges. For example, Rabinovitch (2007a) showed that service thermal loads significantly amplify the stress concentration near the edge of the FRP strip. The amplification of the interfacial stresses raises the question of the impact of the thermal loads on the debonding failure of the beam. This question, which was not addressed in Rabinovitch (2007a), stands in the focus of the present paper.

Along with the CTE mismatch, another inevitable aspect in which the thermal load affects the debonding mechanism is the degradation of the elastic properties of the adhesive. Under temperatures that tend to the glass transition point, this effect probably becomes even more prominent than the CTE mismatch. Kelmar et al. (2008) showed that Young's modulus of the adhesive significantly reduces under temperatures above 40 °C with a glass transition temperature of about Tg = 62 °C (also see Biel and Carlberger, 2007; Carlberger et al., 2009). This effect joins the CTE mismatch and impact the debonding failure of the element.

Opposed to the vast research on the effect of temperature on the behavior of concrete structures with internal FRP reinforcement (e.g. Katz et al., 1999; Katz and Bermal, 2000), the thermal impact on externally strengthened elements received less attention. A comprehensive experimental study on the influence of temperature on strengthened beams was reported by Klamer et al. (2005, 2006a,b, 2008). This study revealed different and sometimes opposite trends in different experimental setups. In double lap shear tests, a temperature rise up to about 50 °C lead to an increase in the debonding load. Beyond that temperature, a notable decrease in the debonding load was observed (Klamer et al., 2005). A similar and even more pronounced effect was also reported by Blontrock (2003) (see in Klamer et al., 2005). On the other hand, Di Tommaso et al. (2001) reported that under four point bending of full scale strengthened beams, the failure load decreased with the increase in temperature.

* Tel.: +972 4 829 3047; fax: +972 4 829 5697.
  E-mail address: cvoded@tx.technion.ac.il
1 Associate Professor and Horev Fellow, supported by the Taub Foundation.

The different and, in some cases, opposite and non-monotonic trends observed in the experiment define an analytical challenge to be faced. The experimental observations also emphasize that the debonding failure involves an interfacial crack initiation and stable/unstable growth. This type of failure mechanism should be treated using a fracture mechanics approach (Rabinovitch, 2004, 2008a; Rabinovitch and Frostig, 2001, Yang et al., 2006, Au and Buyukozturk, 2006, Greco et al., 2007, Carpinteri et al., 2009), a cohesive interface modeling approach (Taljsten, 1996; Wu and Yin, 2003; Yuan et al., 2004; Niu and Wu, 2005; Lu et al., 2005a,b; Wang, 2006a,b; Teng et al., 2006; Ferracuti et al., 2006; Dai et al., 2005; Rabinovitch, 2008b) or a combined fracture mechanics concept with empirically derived parameters (Karbhari et al., 2006).

The use of a fracture mechanics, energy balance, or cohesive interface approaches requires a sound stress analysis model for the thermo-mechanically loaded strengthened beam. Stratford and Cadei (2006) addressed the combined thermal and mechanical loading and presented an analytical model for the evaluation of the adhesion stresses in the strengthened beam. Deng et al. (2004) analytically studied the response of steel beams reinforced with CFRP plates. Thermal strains were also taken into account in the model of Roberts and Haji-Kazemi (1989). In the above models, a linear deformations and uniform shear and vertical normal stresses distributions through the depth of the adhesive layer were assumed. This assumption violates the zero shear condition at the free edge and the equilibrium condition within the adhesive layer. Therefore, it affects the assessment of the stress concentrations near irregular points (edges, cracks, or debonded regions, etc.), see Rabinovitch (2004). A high-order theory that avoids these obstacles was presented by Rabinovitch and Frostig (2000). In this theory, the assumption that the longitudinal stiffness of the adhesive layer is negligible with respect to those of the FRP strip and the concrete beam yields an uniform shear and linear vertical normal stress distributions through the thickness of the adhesive layer. A comparison of the stress fields assessed by this theory with finite element analysis appears in Rabinovitch and Frostig (2000). An augmented model that takes the shear deformations of the adherents into account appears in Hamed and Rabinovitch (2007). The stress fields determined by this model near a cracked and debonded joint in a FRP strengthened masonry wall were also compared with finite element analysis. The comparisons reveal a good agreement between the high-order analysis and the results of the refined finite element analysis but in both cases the thermal effects were not taken into account.

Lovinger (2002) and Lovinger and Frostig (2004) studied the impact of thermal loads on adhesively bonded cladding systems and soft core sandwich plates, respectively. In both cases, a high-order approach that overcomes the above obstacles was used (also see Frostig, 1997). In Lovinger (2002), an energy release rate (ERR) measure was analytically and experimentally defined and a failure criterion replacing the traditional allowable stress approach was applied to the uncracked structure. This study attributed the stability characteristics of the debonding process to the sign of the derivative of the ERR with respect to the crack length and made a distinction between load control and displacement control conditions. In Lovinger and Frostig (2004), the high-order stress analysis under the combined thermal and mechanical loads was applied to a 2D plate type of model. Frostig and Thomsen (2007, 2008a,b) studied the impact of global and localized thermal loads on the geometrically nonlinear response of soft core sandwich panels. The formulation addressed the effect of the thermally induced strains and the degradation of the elastic properties but did not study their impact on the debonding characteristics. A high-order model that accounts for the effect of uniform or linearly varying temperature differentials was presented in Rabinovitch(2007). The results highlighted the amplification of the edge stresses due

to the thermal load. However, the impact of the thermal load on the initiation and the stability characteristics of the debonding failure and the effect of the temperature-dependent properties were not addressed.

A linear fracture mechanics (LFM) model for the simulation of the debonding process in a mechanically stressed beam is presented in Rabinovitch (2008a). This simulation is based on the relation between the load, the displacement, and the crack length under the constraint (failure criterion) of the fracture energy. The results of the LFM were compared with a nonlinear cohesive zone model (Rabinovitch, 2008a,b). The cohesive zone model incorporates nonlinear relations between the tractions (normal and shear) and the displacement jumps across the interface. It also accounts for an interfacial concrete layer may remain attached to the debonded FRP strip after failure. In that sense, it allows for the consideration of a debonding locus within the concrete substrate, a phenomenon that was observed in many experimental studies. The comparison between the LFM model and the nonlinear cohesive fracture model with a thin degraded interfacial layer reveals a reasonable agreement in terms of the overall load deflection path and the ability of the LFM model to describe the stability characteristics of the debonding process. The correlation between the LFM and the nonlinear cohesive interface model also imply that the LFM analysis can potentially overcome the problematic use of stresses that are based on linear analysis for the assessment of failure. The last advantage is gained by a direct application of the ERR (energy balance) criterion without the calibration of strength or failure strain, also see Rabinovitch and Frostig (2001). In that sense, the comparison implies that the LFM model can capture the important aspects of the physical response described by the nonlinear fracture model. It is also noted that in most cases, the concrete layer that is attached to the FRP system is cracked and its contribution to the overall energy balance of the ERR is not expected to be significant. The model and debonding simulation presented in Rabinovitch (2008a) is, however, limited to a single loading system with the advantage of linear and quadratic dependency of the displacements and the energy, respectively, on a single load factor. The procedure does not apply to a combined mechanical and thermal loading or to other combinations of loading systems (see, for example, Rabinovitch, 2007b,c for the assessment of the ERR under combined mechanical and electrical loads of a piezoelectric structure).

The objective of the paper is to gain insight into the impact of the thermal load on the debonding mechanism in beams strengthened with externally bonded FRP strips. To achieve this goal, an analytical model for the thermo-mechanical debonding analysis process is presented. The model focuses on interfacial debonding and assumes that the debonding locus is along the interface of the adhesive layer. The applicability of this modeling assumption is supported by the comparison with the cohesive interface model (Rabinovitch, 2008a) and by the anticipated minor contribution of the cracked and debonded concrete cover layer to the energy balance used in the LFM. The model introduces the thermo-elastic effects through the constitutive modeling and accounts for multiple loading scenarios that stem from the combination of mechanical (gravity) and the thermal loads. In order to focus on the debonding process and its stability characteristics, the model is derived assuming physical and geometrical linearity and a static response. The formulation also assumes that the stress and deformation fields are uniform through the width of each component and that the longitudinal rigidity of the adhesive layer is negligible with respect to the adjacent components.

Another major aspect of the analysis is the variation of the elastic properties and the fracture energy with temperature. It is assumed that the thermal loads are limited to the range where the elastic properties of the concrete and the FRP are independent of the temperature (up to about 100 °C), see Di Tommaso et al. (2001), Saafi

(2002). The temperature dependency of the adhesive (Kelmar et al., 2008) and the degradation of its elastic properties are, on the other hand, taken into account. As for the temperature dependency of the fracture energy, Biel and Carlberger (2007) and Carlberger et al. (2009) experimentally showed that unlike the peak stresses and critical elongations under peel loading, the impact of the temperature of the fracture energy is less sever. These publications reported a slight decrease of about 10% at the highest temperature of 80 °C. Tschegg and Krassnitzer (2008), on the other hand, showed that the fracture energy of a different epoxy paste and its interfacial fracture energy with glass FRP composites reduce by about 18% and 10% at −40 and 45 °C, respectively. Qiao and Xu (2005) reported on a more notable reduction of the fracture energy of the interface between carbon fiber fabrics impregnated with epoxy resin and concrete. They also revealed that in such interface, which is different from the ones in the adhesively bonded pre-fabricated FRP composite, the fracture energy increases under low temperatures, has a local peak at moderately high temperatures (about 55 °C), and decreases at 20–40 °C and after the peak at 55 °C. Although the above observations refer to different materials, material combinations, and interfaces, they imply that the potential dependency of the fracture energy on the temperature should also be considered. This aspect is, therefore, also addressed. It is, however, emphasized that the dependency (or independency) of the properties of the various materials, and therefore the entire analysis, is limited to temperatures that do not significantly exceed the glass transition point. More severe thermal events, much higher temperatures, or fire are not studied here.

2. Mathematical formulation

The mathematical formulation includes three main components. The first one is a stress analysis model that takes the effects of the mechanical and the thermal loads into account. The model follows Rabinovitch (2007a), Frostig (1997), Rabinovitch and Frostig (2000) but takes into account the effect of the temperature on the elastic properties of the adhesive (also see Frostig and Thomsen, 2007, 2008b). For completeness, the relevant parts are outlined in Section 2.1. The second component determines the energy release rate based on the results of the stress analysis model. This part applies the thermo-mechanical form of the *J*-integral (Rice, 1968; Wilson and Yu, 1979; Lei, 2005; Nairn, 2000) for the assessment of the ERR. The third component uses the first two to simulate the equilibrium path of the thermo-mechanical debonding process.

2.1. Stress analysis model

2.1.1. Notation, kinematics, and compatibility/debonding conditions
The notation and the sign conventions appear in Fig. 1. The subscripts "rc", "frp" and "a" refer to the reinforced concrete (RC)

beam, the FRP strip, and the adhesive layer, respectively. The strengthened beam combines different regions that include fully bonded regions, debonded region, and un-strengthened regions. In addition, the formulation makes a distinction between debonded regions in which the interfaces are in contact and debonded regions without such contact.

The kinematic relations for the RC beam and the FRP strip assume small displacements and negligible shear deformation as follows:

$$u_i(x, z_i) = u_{oi} - z_i \beta_i \quad w_i(x, z_i) = w_i \quad \beta_i = w_{i,x}, \tag{1a-c}$$

$$\varepsilon_{xxi} = u_{oi,x} - z_i w_{i,xx}, \tag{2}$$

where $u_{oi} = u_{oi}(x)$, $w_i = w_i(x)$, and $\beta_i = \beta_i(x)$ are the horizontal and vertical displacements and the rotations of the cross section of the RC beam ($i = rc$) and the mid-surface of the FRP strip ($i = frp$), respectively; the coordinate systems (x, z_i) ($i = rc, frp$) are located at the centroid of the cross sections of each component; z_i is measured downwards; and $(\ )_{,x}$ stands for a partial derivative with respect to x. The kinematic relations for the adhesive read:

$$\gamma_{xza} = u_{a,z} + w_{a,x}, \quad \varepsilon_{zza} = w_{a,z}, \tag{3a, b}$$

where u_a and w_a are the adhesive horizontal and vertical displacements, respectively, γ_{xza} is the shear angle, and ε_{zza} is the vertical strain.

The conditions at the adhesive-concrete and adhesive-FRP interfaces are given by:

$$\langle u \rangle = 0 \quad \text{or} \quad \tau_{xz} = 0, \tag{4a, b}$$

$$\langle w \rangle = 0 \quad \text{or} \quad \sigma_{zz} = 0, \tag{5a, b}$$

where $\langle \cdot \rangle$ stands for the jump across each interface and τ_{xz} and σ_{zz} are the shear and normal stresses in the vertical direction. It is emphasized that Eqs. (4,5) apply to each interfaces independently, i.e. the two equations are imposed both at the adhesive-beam interface and at the adhesive-FRP interface. Eqs. (4a) and (5a) stand for a <u>fully bonded</u> interface and impose compatibility of deformations. The zero shear condition Eq. (4b) stands for a <u>debonded</u> interface in which surfaces are free to slip one with respect to another (the effect of friction is neglected). The combination of Eq. (4b) and (5b) yields a <u>debonding without contact</u>. The combination of Eq. (4b) and (5a) yields a <u>debonding with contact</u>. These conditions may vary from one interface to another and along the beam. The length of the debonded region defines the length of the interfacial crack, which controls the debonding process.

2.1.2. Equilibrium equations
The equilibrium equations and the boundary conditions are independent of the thermal effect and thus follow Rabinovitch and Frostig (2000). The equilibrium equations read
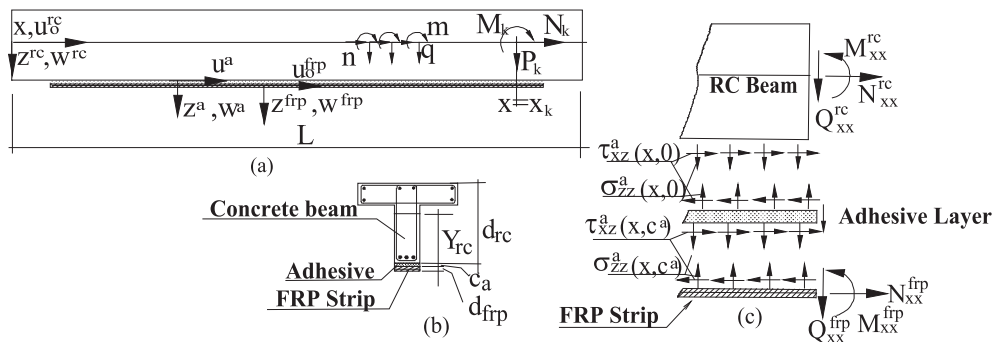

Fig. 1. Notation and sign conventions: (a) coordinate systems and displacements; (b) cross section; (c) interfacial stresses and stress resultants.

$$N_{rc,x} + b\tau_{xza}(x, z_a = 0) + n_{rc} = 0, \tag{6}$$

$$N_{frp,x} - b\tau_{xza}(x, z_a = c_a) + n_{frp} = 0, \tag{7}$$

$$M_{rc,xx} + bY_{rc}\tau_{xza,x}(x, z_a = 0) + b\sigma_{zza}(x, z_a = 0) + q_{rc} = 0, \tag{8}$$

$$M_{frp,xx} + \frac{bd_{frp}}{2}\tau_{xza,x}(x, z_a = c_a) - b\sigma_{zza}(x, z_a = c_a) + q_{frp} = 0, \tag{9}$$

$$\sigma_{zza,z} + \tau_{xza,x} = 0, \tag{10}$$

$$\tau_{xza,z} = 0, \tag{11}$$

where N_{rc} and M_{rc} are the internal stress resultants in the RC beam; N_{frp} and M_{frp} are the internal stress resultants in the FRP strip; n_i and, q_i are distributed external loads at the RC beam ($i = rc$) and the FRP strip ($i = frp$); b is the width of the FRP strip and the adhesive layer; Y_{rc} is the height of the centroid of the cross section of the concrete element above its lower face, d_{frp} is the thickness of the FRP strip; $\sigma_{zza}(x, z_a)$ and $\tau_{xza}(x, z_a)$ are the vertical normal and shear stress fields in the adhesive layer; c_a is the height of the adhesive layer and z_a is the vertical coordinate of the adhesive layer, which is measured from the adhesive-concrete interface downwards (thus $z_a = 0$ stands for the adhesive-concrete interface and $z_a = c_a$ stands for the adhesive-FRP interface). For brevity, the boundary and continuity conditions are not presented here.

2.1.3. Constitutive relations

The total strains defined in Eqs. (2–3) combine the mechanical strains (designated with a superscript M) and the thermal strains (designated with a superscript T) as follows:

$$\varepsilon_{xxrc} = \varepsilon_{xxrc}^M + \varepsilon_{xxrc}^T, \quad \varepsilon_{xxfrp} = \varepsilon_{xxfrp}^M + \varepsilon_{xxfrp}^T, \quad \varepsilon_{zza} = \varepsilon_{zza}^M + \varepsilon_{zza}^T, \tag{12a-c}$$

Assuming a linear strain-temperature relation, the thermally induced strains read:

$$\varepsilon_{xxrc}^T = \alpha_{rc}\Delta T_{rc}(x, z_{rc}), \quad \varepsilon_{xxfrp}^T = \alpha_{frp}\Delta T_{frp}(x, z_{frp}); \quad \varepsilon_{zza}^T = \alpha_a\Delta T_a(x, z_a), \tag{13a-c}$$

$$\Delta T_i(x, z_i) = T_i(x, z_i) - T_{oi}(x, z_i), \tag{14}$$

where α_i are the coefficient of thermal expansion of the concrete element ($i = rc$), the FRP ($i = frp$), and the adhesive ($i = a$), $T_i(x, z_i)$ is the absolute temperature, $T_{oi}(x, z_i)$ is the absolute temperature at the time of curing of the adhesive, and $\Delta T_i(x, z_i)$ is the temperature difference field in each component. The absolute and the relative temperature fields may be represented by any function of the spatial coordinates. It is, however, assumed that this distribution is known and it is independent of the displacements or any other aspect of the structural response.

The constitutive relations for the concrete or the composite material are:

$$\sigma_{xxi} = E_i\varepsilon_{xxt}^M, \tag{15}$$

where E_i is the elastic modulus of a material point in the concrete member ($i = rc$) or in the FRP strip ($i = frp$). Following Di Tommaso et al. (2001) and Saafi (2002), it is assumed that in the range of examined thermal loads, the elastic properties of the concrete and the FRP are not affected by the temperature. Thus, integrating Eq. (15) and using the definitions of the stress resultants yield:

$$N_{rc} = EA_{rc}u_{orc,x} - N_{rc}^T \quad M_{rc} = -EI_{rc}w_{rc,xx} - M_{rc}^T, \tag{16a-b}$$

$$N_{frp} = A_{11frp}u_{ofrp,x} - B_{11frp}w_{frp,xx} - N_{frp}^T;$$
$$M_{frp} = B_{11frp}u_{ofrp,x} - D_{11frp}w_{frp,xx} - M_{frp}^T, \tag{17a-b}$$

where EA_{rc}, EI_{rc} are the inplane and flexural stiffnesses of the RC beam, A_{11frp}, B_{11frp}, D_{11frp} are the stiffnesses of the FRP strip multiplied by its width, and N_i^T, M_i^T equal:

$$\begin{bmatrix} N_i^T \\ M_i^T \end{bmatrix} = \int_{-Y_i}^{d_i - Y_i} b_i E_i \alpha_i \Delta T_i \begin{bmatrix} 1 \\ z_i \end{bmatrix} dz_i \quad (i = rc, frp), \tag{18}$$

where $Y_{frp} = d_{frp}/2$.

The constitutive relations of the adhesive read:

$$\tau_{xza} = G_a\gamma_{xza}, \quad \sigma_{zza} = E_a\varepsilon_{zza}^M = E_a w_{a,z} - E_a\alpha_a\Delta T_a, \tag{19}$$

where G_a and E_a are the shear modulus and the vertical normal elastic modulus of the adhesive, respectively. The elastic properties of the adhesive layer may depend on the temperature and therefore, in the general case, they read:

$$E_a = E_a(T_a(x, z_a)) = E_a(x, z_a), \quad G_a = G_a((T_a(x, z_a)) = G_a(x, z_a), \tag{20a, b}$$

where the temperature field $T_a = T_a(x, z_a)$ and the temperature-elastic moduli relations are known a priori and assumed independent of the mechanical response.

2.1.4. Adhesive layer – stress and displacement fields

The derivation of the stress and the displacement fields in the adhesive layer adopt the concepts of the high-order theory (Rabinovitch and Frostig, 2000) while taking into account the thermal effects and the degradation of the elastic properties (also see Frostig and Thomsen (2007, 2008a,b)).

The integration of Eqs. (11–12) yields:

$$\tau_{xza}(x, z_a) = \tau_{xza}(x) = \tau_a, \tag{21}$$

$$\sigma_{zza}(x, z_a) = -\tau_{a,x}z_a + F_1(x), \tag{22}$$

where $F_1(x)$ is a function of x only.

If the two interfaces are fully bonded, the shear stress is uniform through the depth of the adhesive layer and the vertical normal stress is linear (also see Rabinovitch and Frostig, 2000)). If one of the interfaces is debonded but the damaged surfaces are in contact, the zero shear condition, Eq. (4b), yields zero shear stresses and uniform normal stress through the depth of the layer. If the debonded interfaces are not in contact Eq. 5b, both the shear and the normal stress σ_{zza} vanish.

By means of Eq. (21), the kinematic relation, Eq. (3b), the constitutive law, Eq. (19), and by assuming that E_a and G_a do not totally vanish, the vertical displacement of the adhesive takes the following form:

$$w_a(x, z_a) = -\tau_{a,x} \cdot f_1(x, z_a) + F_1(x) \cdot f_0(x, z_a) + F_2(x) + \theta(x, z_a), \tag{23}$$

where $F_2(x)$ is a function of x only and $\theta(x, z_a), f_0(x, z_a)$ and $f_1(x, z_a)$ are given by:

$$f_0(x, z_a) \equiv \int_0^{z_a} \frac{1}{E_a(T_a(x, \zeta_a))} d\zeta_a, \quad f_1(x, z_a) \equiv \int_0^{z_a} \frac{\zeta_a}{E_a(T_a(x, \zeta_a))} d\zeta_a, \tag{24-25}$$

$$\theta(x, z_a) \equiv \int_0^{z_a} \alpha_a\Delta T_a(x, \zeta_a) d\zeta_a, \tag{26}$$

where ζ_a is a dummy integration variable that replaces z_a in the fields $T_a(x, \zeta_a)$ and $E_a(T_a(x, \zeta_a))$, thus the integrals yield functions of z_a.

In the cases of a full bonding or debonding with contact, $F_1(x)$ and $F_2(x)$ are determined by the independent evaluation of the compatibility condition Eq. (5a) at both interfaces. This yields

$$\sigma_{zza}(x, z_a) = \frac{w_{frp} - w_{rc}}{f_0^c(x)} + \tau_{a,x}\left(\frac{f_1^c(x)}{f_0^c(x)} - z_a\right) - \frac{\theta^c(x)}{f_0^c(x)}, \tag{27}$$

$$w_a(x, z_a) = \tau_{a,x}(h_1(x, z_a) - f_1(x, z_a)) + (w_b - w_t)h_0(x, z_a) + w_t + \theta(x, z_a) - \psi(x, z_a), \tag{28}$$

where the superscript "c" indicates a function evaluated at $z_a = c_a$, i.e. $f^c(x) = f(x, z_a = c_a)$ and

$$h_0(x, z_a) \equiv \frac{f_0(x, z_a)}{f_0^c(x)} \quad h_1(x, z_a) \equiv f_0(x, z_a)\frac{f_1^c(x)}{f_0^c(x)},$$

$$\psi(x, z_a) \equiv f_0(x, z_a)\frac{\theta^c(x)}{f_0^c(x)}, \tag{29-31}$$

In the case of debonding with contact, τ_a, and $\tau_{a,x}$ in Eqs. (27), (28) vanish. In case of debonding without contact, $\sigma_{zza}, F_1(x)$, τ_a, and $\tau_{a,x}$ vanish and $F_2(x)$ is determined based on the compatibility conditions Eq. (5a) evaluated at the single fully bonded interface.

The longitudinal displacement field is determined by integrating the kinematic assumption of Eq. (3a). In the fully bonded case, it reads:

$$u_a(x, z_a) = \tau \cdot g_0(x, z_a) + \tau_{,x} \cdot g_{1,x}(x, z_a) + \tau_{,xx} \cdot g_1(x, z_a) - (w_{frp,x} - w_{rc,x}) \cdot g_2(x, z_a) - (w_{frp} - w_{rc}) \\ \cdot g_{2,x}(x, z_a) + u_{orc} - (Y_{rc} + z_a)w_{rc,x} + \chi(x, z_a), \tag{32}$$

where

$$g_1(x, z_a) \equiv \int_0^{z_a} (f_1(x, \zeta_a) - h_1(x, \zeta_a))d\zeta_a,$$

$$g_2(x, z_a) \equiv \int_0^{z_a} h_0(x, \zeta_a)d\zeta_a, \tag{33-34}$$

$$g_0(x, z_a) \equiv \int_0^{z_a} \frac{1}{G_a(x, \zeta_a)}d\zeta_a;$$

$$\chi(x, z_a) \equiv \int_0^{z_a} (\psi_{,x}(x, \zeta_a) - \theta_{,x}(x, \zeta_a))d\zeta_a. \tag{35-36}$$

If one of the interfaces is debonded but vertical contact exists, τ_a and $\tau_{a,x}$ in Eq. (32) vanish. If the adhesive-FRP interface is debonded without contact, the longitudinal displacement reads:

$$u_a(x, z_a) = -w_{rc,x}z_a + u_{orc} - Y_{rc}w_{rc,x} + \chi(x, z_a). \tag{37}$$

If the adhesive-concrete interface is debonded without contact, it reads:

$$u_a(x, z_a) = (w_{frp,x} - w_{rc,x})(g_2^c(x) - g_2(x, z_a)) + (w_{frp} \\ - w_{rc})(g_{2,x}^c(x) - g_{2,x}(x, z_a)) + u_{orc} - (Y_{rc} + z_a \\ - c_a)w_{rc,x} + \chi(x, z_a) - \chi^c(x). \tag{38}$$

The above formulation refers to a general temperature field $T(x, z)$. Specific expressions for the case of linear variation with z and their impact on the geometrically nonlinear response of sandwich panels appear in Frostig and Thomsen (2007). In the case of the FRP strengthened beam studied here, the variation of the temperature through the thickness of the adhesive layer and, in turn, the variation of the elastic moduli through the thickness, are practically less significant. On the other hand, the variation in the x direction due to localized thermal loads may be of practical significance and interest.

2.1.5. Governing equations

The governing equations are stated in terms of u_{ot}, w_t, u_{ob}, w_b, and τ_a as follows:

$$EA_{rc}u_{orc,xx} + b\tau_a = -n_{rc} + N_{rc,x}^T \tag{39}$$

$$A_{11frp}u_{ofrp,xx} - B_{11frp}w_{frp,xxx} - b\tau_a = -n_{frp} + N_{frp,x}^T \tag{40}$$

$$-EI_{rc}w_{rc,xxxx} + b\left(\frac{f_1^c(x)}{f_0^c(x)} + Y_{rc}\right)\tau_{a,x} + b\frac{w_{frp} - w_{rc}}{f_0^c(x)} \\ = -q_{rc} + M_{rc,xx}^T + \frac{\theta^c(x)}{f_0^c(x)} \tag{41}$$

$$- D_{11frp}w_{frp,xxxx} + B_{11frp}u_{ofrp,xxx} + b\left(\frac{d_{frp}}{2} - \frac{f_1^c(x)}{f_0^c(x)} + c_a\right)\tau_{a,x} \\ - b\frac{w_{frp} - w_{rc}}{f_0^c(x)} = -q_{frp} + M_{frp,xx}^T - \frac{\theta^c(x)}{f_0^c(x)}, \tag{42}$$

$$u_{orc} - u_{ofrp} + \tau_a g_0^c - g_1^c(x)\tau_{a,xx} - g_{1,x}^c(x)\tau_{a,x} - (c_a - g_2^c(x) + Y_{rc})w_{rc,x} \\ - \left(g_2^c(x) + \frac{d_{frp}}{2}\right)w_{frp,x} - (w_{rc} - w_{frp})g_{2,x}^c(x) + \chi^c(x) = 0. \tag{43}$$

Eq. (43) stems from the compatibility conditions, Eq. (4a), imposed at the adhesive-FRP interface. In the debonded regions, Eq. (4a) is replaced with Eq. (4b) and, in the light of Eqs. (11) and (21), Eq. (43) is replaced with the zero shear stress condition. Consequently, Eq. (43) and all the terms that include τ_a and its derivatives vanish. If the debonding is without contact, all terms associated with the vertical normal stress vanish as well.

The governing equations form a set of linear ordinary differential equations with variable coefficients. In the general case, the elastic properties depend on the temperature and coordinates, a general closed form solution does not exist, and a numerical solution is applied. The solution of the governing equations provides the basis for the fracture analysis stage, which is discussed next.

2.2. Fracture analysis

The interfacial debonding initiation and growth criterion adopts the concept of the energy balance and require that the energy release rate (ERR), G, equals the fracture energy, G_c. G is evaluated using the J-integral (Rice, 1968; Wilson and Yu, 1979) or through the finite difference derivative of the total energy. Following the formulation presented in Lei (2005), the J-integral for the two dimensional (x and z) case and a crack directed along the x-axis of the mechanically and thermally stressed body reads:

$$G = J = \int_\Gamma \left(W\delta_{1i} - \sigma_{ij}\frac{\partial u_j}{\partial x_1}\right)n_i ds + \int_A \sigma_{ii}\frac{\partial \varepsilon^T}{\partial x_1}dA, \tag{44}$$

where Γ is the path surrounding the crack tip, A is the area surrounded by Γ, σ_{ij} are the components of the stress tensor, $x_1 = x$ and $x_2 = -z$ are the spatial coordinates, δ_{ij} is Kronecker's delta, and W is the mechanical strain energy density function:

$$W = \int_0^{\varepsilon_{ij}^M} \sigma_{ij}d\varepsilon_{ij}^M. \tag{45}$$

The stress, strain, deformation, and energy density fields are obtained by the stress analysis model. The J integral of Eq. (44), which differs from the one adopted in Rabinovitch and Frostig (2001) for the mechanically loaded beam, is path independent also under the thermal traction.

2.3. Debonding growth simulation

The debonding process takes the form of an equilibrium surface in the load-displacement-temperature space under the constraint:

$$G(\mathbf{u}, \lambda^M, \lambda^T) - G_c = 0, \tag{46}$$

where λ^M is a mechanical load factor that scales <u>all</u> mechanical loads, λ^T is a thermal load factor that scales <u>all</u> thermal load (i.e. the temperature difference field), $\mathbf{u} = \mathbf{u}(\mathbf{x})$ is the displacement field; and $\mathbf{x}$ designates the spatial coordinates or a specific point that is of interest. The procedure for the evaluation of the equilibrium path under the combined mechanical and thermal load is discussed next. The particular case where the beam is only subjected to a mechanical load is studied in Rabinovitch (2008a).

Eq. (46) implicitly assumes that the fracture energy G_c is independent of the temperature. The case where this assumption does not hold and G_c is a function of temperature is addressed at the end of this section.

The debonding growth simulation takes advantage of the linearity of the stress analysis model. In case the temperature does not affect the elastic properties of the adhesive, the displacements response is linear in both the mechanical load factor λ^M and the thermal load factor λ^T and the ERR is quadratic in the two load factors. In that case, the procedure outlined next can be directly used. If the elastic moduli depend on the temperature, the linearity with respect to λ^T vanishes and the applicability of the procedure is limited to the specific thermal load factor used for the formulation. It is also assumed that the type of debonding (with or with out contact) dose not change through the process. The thermo-mechanical debonding simulation is as follows:

1. Define a series of debonding lengths, $\mathbf{a} = [a_i]$ ($i = 1 \ldots N_a$) ranging from zero and up to complete detachment. Also, define the type of debonding.
2. For the i'th debonding length, a_i:
   2.1 Solve the stress analysis model with the length of debonded region $= a_i$ under an <u>arbitrary magnitude</u> of external load $\bar{\lambda}^M$ and <u>zero</u> thermal load $\lambda^T = 0$. Evaluate the ERR and the displacement field corresponding to a_i and $\bar{\lambda}^M$:

$$\overline{G}_i^M = G(a_i, \lambda^M = \bar{\lambda}^M, \lambda^T = 0). \tag{47}$$

$$\bar{\mathbf{u}}_i^M = \mathbf{u}(a_i, \lambda^M = \bar{\lambda}^M, \lambda^T = 0). \tag{48}$$

   (In the following, the over-bar designates arbitrary load factors or quantities obtained using the arbitrary factors)
   2.2 Solve the stress analysis model (with a_i) under an <u>arbitrary magnitude</u> of thermal load $\bar{\lambda}^T$ and <u>zero</u> mechanical load $\lambda^M = 0$. Evaluate the ERR and the displacement fields corresponding to a_i and $\bar{\lambda}^T$:

$$\overline{G}_i^T = G(a_i, \lambda^M = 0, \lambda^T = \bar{\lambda}^T) \tag{49}$$

$$\bar{\mathbf{u}}_i^T = \mathbf{u}(a_i, \lambda^M = 0, \lambda^T = \bar{\lambda}^T) \tag{50}$$

   2.3 Solve the stress analysis model (with a_i) under <u>arbitrary magnitudes</u> of both the thermal load $\bar{\lambda}^T$ and the mechanical load $\bar{\lambda}^M$. Evaluate the ERR corresponding to $a_i, \bar{\lambda}^M \quad \bar{\lambda}^T$:

$$\overline{G}_i^{TM} = G(a_i, \lambda^M = \bar{\lambda}^M, \lambda^T = \bar{\lambda}^T). \tag{51}$$

3. Use the vectors $\overline{\mathbf{G}}^{\mathbf{M}} = [\overline{G}_i^M]; \overline{\mathbf{G}}^{\mathbf{T}} = [\overline{G}_i^T]; \overline{\mathbf{G}}^{\mathbf{TM}} = [\overline{G}_i^{TM}]; \bar{\mathbf{u}}^{\mathbf{M}} = [\bar{\mathbf{u}}_i^M]; \bar{\mathbf{u}}^{\mathbf{T}} = [\bar{\mathbf{u}}_i^T]$ that correspond to the vector $\mathbf{a} = [a_i]$ and the arbitrary magnitudes $\bar{\lambda}^M, \bar{\lambda}^T$ to construct the functions $\overline{G}^M(a), \overline{G}^T(a), \overline{G}^{TM}(a), \bar{\mathbf{u}}^M(a), \bar{\mathbf{u}}^T(a)$ using a curve fitting algorithm.
4. Using the linear and the quadratic forms, the displacements and the ERR under <u>any magnitude</u> of loads $\underline{\lambda}^T \underline{\lambda}^M$ read:

$$\mathbf{u}(a, \lambda^T, \lambda^M) = \bar{\mathbf{u}}^T(a) \frac{\lambda^T}{\bar{\lambda}^T} + \bar{\mathbf{u}}^M(a) \frac{\lambda^M}{\bar{\lambda}^M} \tag{52}$$

$$G(a, \lambda^T, \lambda^M) = \overline{G}^T(a) \left(\frac{\lambda^T}{\bar{\lambda}^T}\right)^2 + \overline{G}^M(a) \left(\frac{\lambda^M}{\bar{\lambda}^M}\right)^2$$
$$+ \left(\overline{G}^{TM}(a) - \overline{G}^T(a) - \overline{G}^M(a)\right) \frac{\lambda^M \lambda^T}{\bar{\lambda}^M \bar{\lambda}^T} \tag{53}$$

As mentioned at the beginning of the section, Eqs. (52), (53) are valid in the temperature range where all elastic moduli are independent of the temperature. Otherwise, the expressions are valid only for the thermal load level used for the analysis $\lambda^T = \bar{\lambda}^T$ and Eqs. (52), (53) reduce to:

$$\mathbf{u}(a, \lambda^M) = \bar{\mathbf{u}}^T(a) + \bar{\mathbf{u}}^M(a) \frac{\lambda^M}{\bar{\lambda}^M}, \tag{54}$$

$$G(a, \lambda^M) = \overline{G}^T(a) + \overline{G}^M(a) \left(\frac{\lambda^M}{\bar{\lambda}^M}\right)^2$$
$$+ \left(\overline{G}^{TM}(a) - \overline{G}^T(a) - \overline{G}^M(a)\right) \frac{\lambda^M}{\bar{\lambda}^M}. \tag{55}$$

In case the elastic moduli and the fracture energy are independent of the temperature, the equilibrium surface is defined by Eqs. (52), (53) and the constraint, Eq. (46). This yield a surface with the general form $\psi(\mathbf{u}, \lambda^M, \lambda^T) = 0$. If the elastic properties and/or the fracture energy depend on the temperature, Eqs. (54), (55) are used and the constraint of Eq. (46) is evaluated with $G_c = G_c(\bar{\lambda}^T)$. In this case, $\bar{\lambda}^T$ is not arbitrary but it represents the relevant level of thermal load. The equilibrium surface then collapses to an equilibrium path $\psi(\mathbf{u}, \lambda^M) = 0$ that is valid for the specific $\bar{\lambda}^T$ only. In both cases, the equilibrium surface or the equilibrium path are given in a parametric form with the crack length a being the parameter (in the mathematical sense), also see Carpinteri (1985) and Carpinteri and Monetto (1999). The shape of the surface (or its 2D projection in case one type of load is prescribed) defines the stability characteristics of the debonding process.

3. Numerical study

The numerical study includes two cases. First, the double lap shear specimen experimentally studied by Klamer et al. (2005, 2006a,b, 2008) is examined. The comparison aims to validate the model and explain some of the interesting phenomena observed in the experiments. The second case studies a simply supported FRP strengthened RC beam subjected to a combination of mechanical and thermal loads.

3.1. Comparison with experiments

The geometry and the mechanical properties of the specimen follow Klamer et al. (2005, 2006a,b, 2008) and appear in Fig. 2. The specimen is subjected to an uniform temperature change with respect to a reference temperature of T = 20 °C and to mechanical loads at the ends. The specimen includes as pre-formed 50 mm long debonded region near the saw-cut at the middle. In order to simplify the analysis, symmetry conditions are adopted and 1/4 of the doubly symmetric specimen (Fig. 2(c)) is analyzed. The elastic modulus of the concrete prism and the equivalent elastic modulus of the unidirectional FRP strip are assumed temperature independent and equal E^{rc} = 32.35 GPa and E^{frp} = 165 GPa, respectively. The coefficients of thermal expansion of the concrete, FRP, and adhesive are α_{rc} = 11·10⁻⁶[1/°C], α_{frp} = 0.3·10⁻⁶[1/° C], and α_a = 90·10⁻⁶[1/°C], respectively. The fracture energy, G_c = 928 J/m², was calibrated using the experimental results given for series A at the reference temperature (Klamer et al., 2005). With the absence of specific information regarding the temperature dependency of the fracture energy for the particular case at hand, the analysis first follows Biel and Carlberger (2007) and Carlberger et al. (2009) and assumes that the fracture energy is independent of the temperature. The impact of the reduction in the fracture energy under low and elevated temperatures reported by Tschegg and Krassnitzer (2008) for a different epoxy adhesive and interface is then assessed. Following Kelmar et al. (2008), the elastic and shear moduli of the adhesive layer, which depend on the temperature, are given is Table 1. Due to the temperature dependency, the simulation of the debonding process requires re-evaluation of the path for every examined temperature through Eqs. (54), (55).
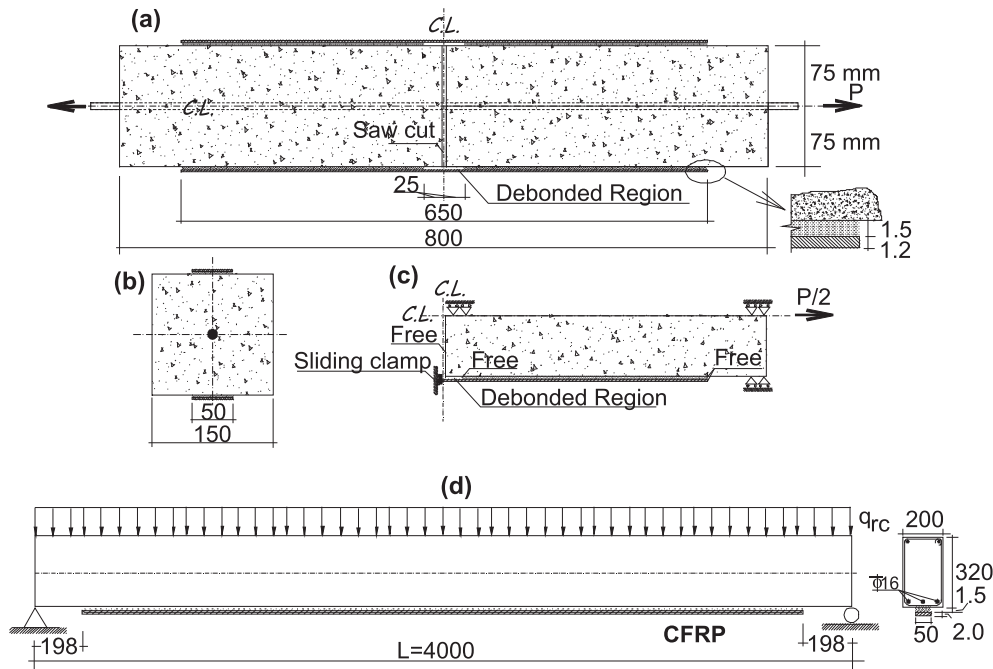
Fig. 2. Geometry (not to scale) and mechanical loading for the numerical study: (a) Double lap shear specimen adapted from Klamer et al. (2005); (b) Cross section of the double lap shear specimen; (c) 1/4 of the doubly symmetric double lap shear specimen (d) Strengthened simplify supported beam.

Table 1
Temperature dependent elastic and shear moduli of the adhesive (adapted form Kelmar et al. (2008)).

Temperature [°C]	⩽20	30	40	50	60	70	80
E_a [MPa]	12,800	12,000	10,400	6,700	1,000	50.0	10.00
G_a [MPa]	4,925	4,615	4,000	2,575	385	19.2	3.85

The most interesting finding of the experimental program reported in Klamer et al. (2005) is the pattern of the dependency of the debonding failure load on the temperature. This is also reflected by the experiments reported in Blontrock (2003) and discussed in Klamer et al. (2005). To examine this unique aspect, the results are presented in terms of the entire debonding path at different temperatures and in terms of the debonding initiation load versus temperature.

The equilibrium paths for the double lap shear test under T = −10, 20, and 50 °C and constant fracture energy appear in Fig. 3. Two families of paths are presented. The first one (Fig. 3(a)) stands for a debonding process that initiates near the saw-cut at the middle of the specimen and propagates towards the edge (Inner debonding). The second group of paths (Fig. 3(b)) stands for a debonding process that initiates near the edge of the bonded FRP strip and propagates towards the middle (Edge Debonding). The curves show that the two types of debonding process are unstable. Therefore, it is expected that the initiation of the debonding immediately leads to a total peel off failure, regardless of the temperature and the point of initiation. This observation is in agreement with the experimental results reported in Klamer et al. (2005). Fig. 3 also indicates that up to the higher examined temperatures, the edge debonding initiation load is considerably higher than the inner debondign load. This indicates that the inner debonding, which is triggered by the lower failure load among the two, is expected to happen way before the edge debonding. The extremely high (and evidently nonrealistic) failure loads attributed to the edge debonding are therefore theoretical only.

The thermal effect studied in Fig. 3 shows that the temperature increase shifts the inner debonding path upwards and increases the "strength" of the specimen. On the other hand, it shifts the edge debonding path downwards and decreases the edge debonding strength. These effects are further studied in terms of the debonding failure load versus temperature curves next.

The theoretical and experimental failure load versus temperature results are studied in Fig. 4. Fig. 4(a) refers to inner debonding and Fig. 4(b) refers to the edge debonding. The experimental results are taken from Klamer et al. (2005) and refer to test series A (tested at T = 20, 50, and 75 °C) and C (tested at T = 20 and − 10 °C). G_c was calibrated using the results of series A at T = 20 °C and kept constant yielding the asterisks (connected by dotted lines) in Fig. 4. The crosses that are connected by the thin dashed lines result from the analysis that accounts for the temperature effect on the fracture energy as well. The comparison between the analytical and the experimental results in Fig. 4(a) shows that the analytical model captures the increase in the inner debonding load up to about 60 °C and then the decrease in the failure load under higher temperatures. Both effects were observed in the experimental study (Klamer et al., 2005). It is also observed that the analytical values are in reasonable agreement with the experimental ones.

The results in terms of the edge debonding loads versus temperature appear in Fig. 4(b). Up to 60 °C, the predicted failure loads are significantly higher than the ones due to inner debonding (Fig. 4(a)) and therefore an edge debonding failure is not expected. On the other hand, the edge failure load monotonically decreases with the increase in temperature. Under temperatures higher than 60 °C and a notable reduction in the elastic properties of the adhesive, the predicted edge debonding load drops down to the levels observed in the experiment. This implies that under the higher temperatures, the debonding may have initiated at the edge of the FRP strip rather than near the inner saw-cut.

Another aspect that affects the assessment of the temperature impact on the failure is the potential dependency of the fracture energy on the temperature. With the absence of experimental
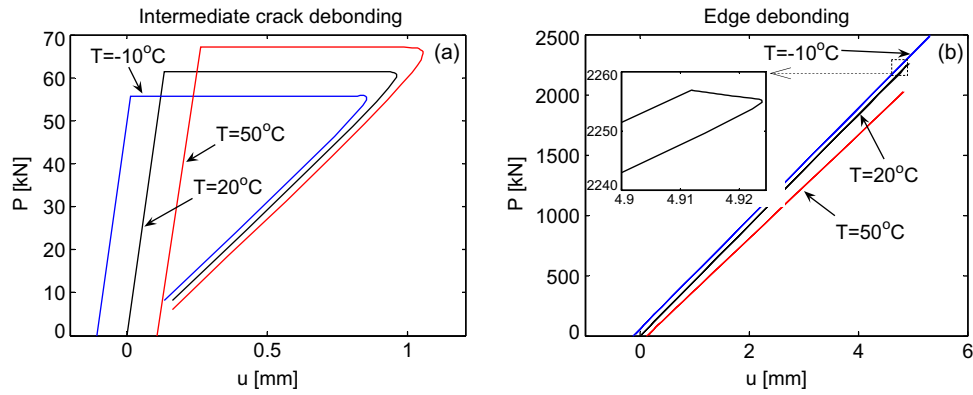
Fig. 3. equilibrium path for the double lap shear test under different temperatures: (a) Intermidiate crack debonding process; (b) Edge debonding process.
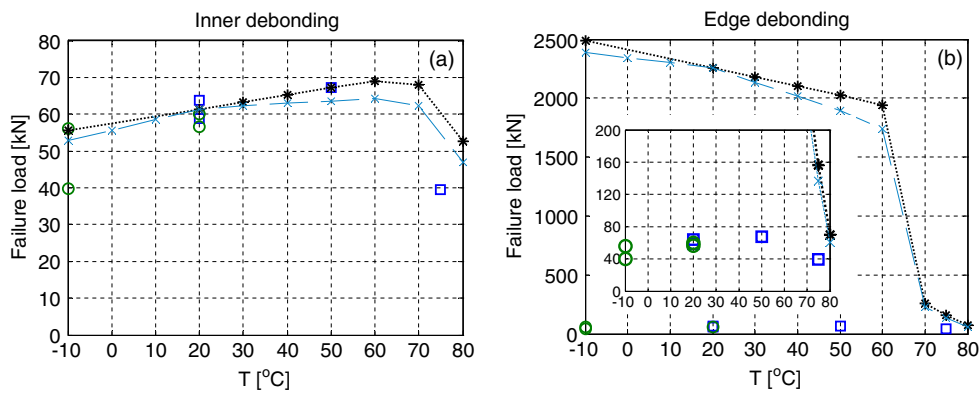

Fig. 4. Analytical prediction and experimental failure load vs. temperature response in double lap shear test: (a) Inner debonding (b) Edge debonding. (Legend: □ Experimental, series A (adapted from Klamer et al., 2005), ○ Experimental, series C (adapted from Klamer et al., 2005) ...*... Analysis – temperature independent fracture energy; –x– temperature dependent fracture energy).

characterization of the fracture energy versus temperature relation for the particular case at hand, the results assuming temperature independent fracture energy appear in black asterisks connected by dotted lines in Fig. 4. Tschegg and Krassnitzer (2008), on the other hand, reported a reduction in G_c for other epoxy adhesives and interfaces with the increase and with the decrease of temperature. Quantitatively, they report an average reduction of about 18% at −40 °C and an average reduction of about 10% at +45 °C (both with respect to the value at room temperature). A higher reduction factor for elevated temperatures, but an increase in fracture energy at about 55 °C and at lower temperatures was reported by Qiao and Xu (2005) but for a different material combination of epoxy impregnated carbon fabric and concrete. Adopting the reduction factors reported by Tschegg and Krassnitzer (2008) and a linear interpolation/extrapolation yields the crosses connected with thin dashed lines shown in Fig. 4. These results and the consideration of the reduction in G_c reveal a better correlation with the experimental results at the ends of the examined temperature range. It is further expected that near the glass transition point, the reduction in G_c would become even more prominent then the one based on linear extrapolation (see, for example, Qiao and Xu, 2005). This trend would further lessen the differences between the analytical prediction and the experimental results at higher temperatures. It is, however, emphasized that the reduction factors used in the analysis were not specifically derived for the particular case at hand and, therefore, should be considered as a rough estimation of the anticipated trends only.

In order to further study the difference between the inner debonding and the edge debonding under thermo-mechanical load,

the interfacial stress distributions are examined. The distributions near the end of the debonded region pre-formed in the vicinity of the saw-cut and near the edge of the FRP system under a pull out load of 35 kN and a temperature rise of 30 °C (applied separately) appear in Fig. 5. Near the inner debonding, the interfacial stresses due to the mechanical load and due to the thermal load are of opposite signs. The thermal effect therefore tends to cancel the interfacial stresses due to the mechanical loads. This explains the increase in the failure load observed in the experiments up to T = 60 °C. Beyond this temperature, the reduction in the elastic properties of the adhesive yields the reduction in the failure load observed in the experiment and in the analytical results of Fig. 4(a).

The interfacial stresses near the edge show a different trend. There, the stresses due to the mechanical load and the thermal load are of the same sign. Therefore, the thermal stresses amplify the shear and the peeling stresses at the adhesive-concrete interface and reduce the failure load (Fig. 4(b), Klamer et al., 2005). The reduction in the elastic properties of the adhesive further decrease the predicted failure load leading to the steep reduction predicted above 60 °C.

The different trends detected in Fig. 5 also throw some light on the different modes of failure reported in the experimental program of (Klamer et al., 2005, 2006b). The mode of failure shifted from failure in the concrete with a few millimeters thick concrete layer attached to the FRP strip at room temperature to failure at the adhesive-concrete interface at elevated temperatures. Fig. 5(a) shows that at room temperature, the adhesive-concrete interface near the inner crack is subjected to compression whereas the more resilient adhesive-FRP interface is subjected to peeling (tensile)
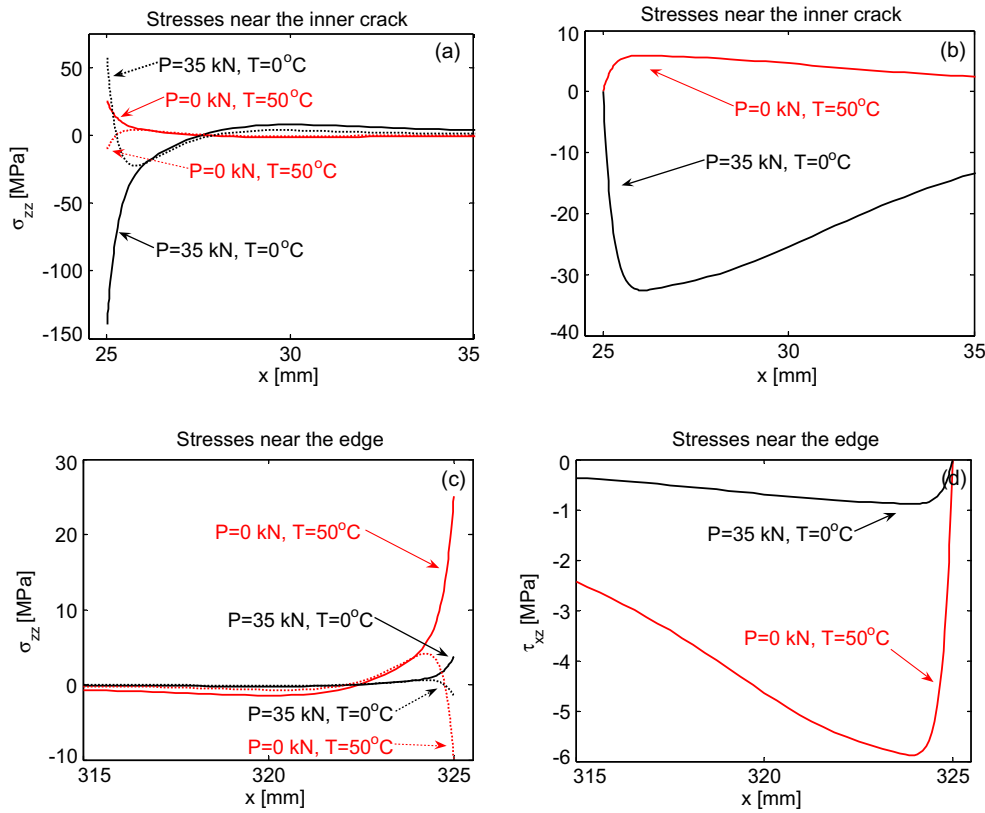
Fig. 5. Vertical normal and shear stresses under mechanical (P = 35 kN) and thermal (T = 50 °C) loads (applied separately): (a) normal stresses near the inner debonding; (b) shear stresses near the inner debonding (c) normal stresses near the edge; (d) shear stresses near the edge (Legend for normal stresses: —— = adhesive-concrete interface; ...... adhesive-FRP interface).

stresses. Under such conditions, the shear stresses become critical and contribute to the evolution of failure in the concrete cover layer starting at the inner crack and propagating towards the edges. Under the elevated temperature, on the other hand, the vertical normal peeling stresses that develop at the adhesive-concrete interface near the edge are significantly amplified. This effect, the reduction in the elastic properties of the adhesive, and the potential reduction in the fracture energy trigger a failure in the tensioned adhesive-concrete interface. Such failure was observed in the experiment. It should, however, be noted that the analysis refers to debonding at the adhesive-concrete interface only. Yet, the comparison between the interfacial failure and a cohesive failure within the concrete member itself modeled using nonlinear fracture analysis (Rabinovitch, 2008a,b) indicate that the presence of the thin concrete layer due to debonding locus within the concrete substrate does not significantly changes the predicted failure path.

Finally, the analytical and the experimental results are compared in terms of the strains along the outer face of the FRP strip. The strains were experimentally measured using 10 mm long strain gauges located at 10, 80, 150, 210, and 280 mm from the end of the laminate. The distributions of the strain are compared in Fig. 6. Two sets of results are examined. The first one corresponds to the reference temperature T = 20 °C and the second one to T = 75 °C. The comparison reveals a good agreement between the analytical and the experimental results. The analytical model captures the change in the strain distribution due to the temperature rise and the deterioration of the elastic properties of the adhesive. The softening of the adhesive reduces the effectiveness of the stress transfer between the components and therefore relaxes the steep development of the strains near the loaded edge. Fig. 6 also shows that the resolution of the measurements with the

strain gauges is limited. In that sense, the analytical results complement the experimental ones. For example, with the absence of direct measurements, the analytical model quantifies the localized bending strains near the inner debonded region and the impact of the thermal load on them.

3.2. Thermal impact on edge debonding

The geometrical properties of the 4.0 long Carbon FRP strengthened reinforced concrete (RC) beam appear in Fig. 2(d). The elastic properties of the concrete, the adhesive, and the FRP, and the CTEs are the same as in the previous example, yet the properties of the
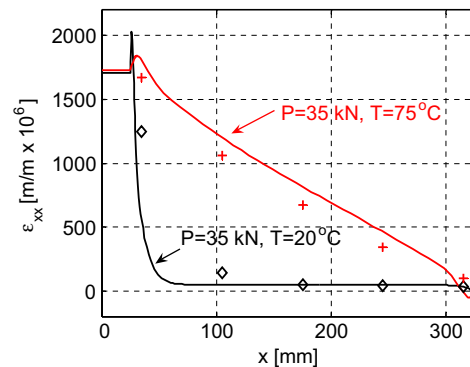

Fig. 6. Strains along the outer face of the FRP strip under P = 35 kN and different temperatures. (Legend: —analytical T = 20 °C; — analytical T = 75 °C; ◇◇ experimental T = 20 °C; ++ experimental T = 75 °C) Experimental results adapted from Klamer et al. (2005).

cracked cross section of the RC beam are adopted. In this example, $G_c = 950$ J/m^2 and, in the light of the discussion brought up above and the lack of specific experimental data, it is assumed that the fracture energy is independent of the temperature. The beam is subjected to a uniformly distributed load and an uniform temperature change.

The equilibrium paths under different temperatures appear in Fig. 7. The points along line ABC refer to the structure before debonding (i.e. a = 0). Point C is the first one that satisfies the constraint of the fracture energy (Eq. (46)) and therefore designates the initiation of the debonding process. In all cases, the equilibrium path includes an unstable branch along points C–D. This branch reflects the unstable debonding process governed by a snap through and a sudden increase in deformations under load control or a snap back and a sudden drop in load under displacement control (also see Rabinovitch (2008a,b) and Carpinteri et al. (2009), both referring to mechanically stressed beams). Beyond point D, the debondign process continues in a stable meaner towards point E with the final slope of the curve DE designating the stiffness of the debonded beam. The sudden snap and, in some cases, the potential crack arrest along branch DE (after a significant growth of the interfacial crack though) were experimentally observed (see, for example, Rabinovitch and Frostig, 2003, 2006).

The equilibrium paths of Fig. 7 show that the thermal load alters the snap point and therefore the debonding strength. Under the studied conditions, which can all be considered in the range of standard service thermal loads, the temperature rise to 50 °C reduces the critical load level by almost 17% (see Fig. 7(e)–(f) compared with Fig. 7(c) and (d)). On the other hand, when the temperature drops to −10 °C, the debonding strength is expected to increase by about 9% (see Fig. 7(a)–(b)). The reduction of the debonding strength under normal thermal loads conditions has a critical impact on the structural performance of the element. Therefore, it should be considered in the design and analysis procedures.

4. Summary and conclusions

The influence of thermal loads on the debonding failure in beams strengthened with externally bonded composite materials has been analytically investigated. The analytical approach has included a high order stress analysis model that incorporates the thermally induced effects and a fracture mechanics model that uses the J integral formulation and its augmentation to the thermo-mechanical case. The two models have been combined for the synthesis of the equilibrium surface and for the simulation of the interfacial crack initiation and propagation process.

The analytical capabilities have been validated through comparison with experimental results taken from the literature. The analysis of a double lap shear specimen subjected to mechanical and thermal load has revealed a good agreement with the experimental results. A correlation has been observed in the terms of the impact of the thermal load on the pre-deboning strain field and the debonding failure load. The analysis has quantified and explained some of the various phenomena observed in the experiments. In particular, it has captured and quantified the stability characteristics and initial increase and then the decrease in the debonding failure load. The analytical results have shown that this non-monotonic trend is affected by the thermal impact on the interfacial stresses, the inherently different stress fields near an inner crack and near the edge of the bonded system, the thermal degradation of the elastic properties of the adhesive, and, potentially, the thermal degradation of the fracture energy.

The analytical approach has been adopted for the numerical study of the impact of a thermal load on the debonding initiation, growth, and stability in a simply supported strengthened beam. The results have revealed a reduction in the anticipated snap load and a reduction in the load level designating the transition to instability. This trend has pointed at a reduction in the debonding strength with the increase in temperature, even in cases that are
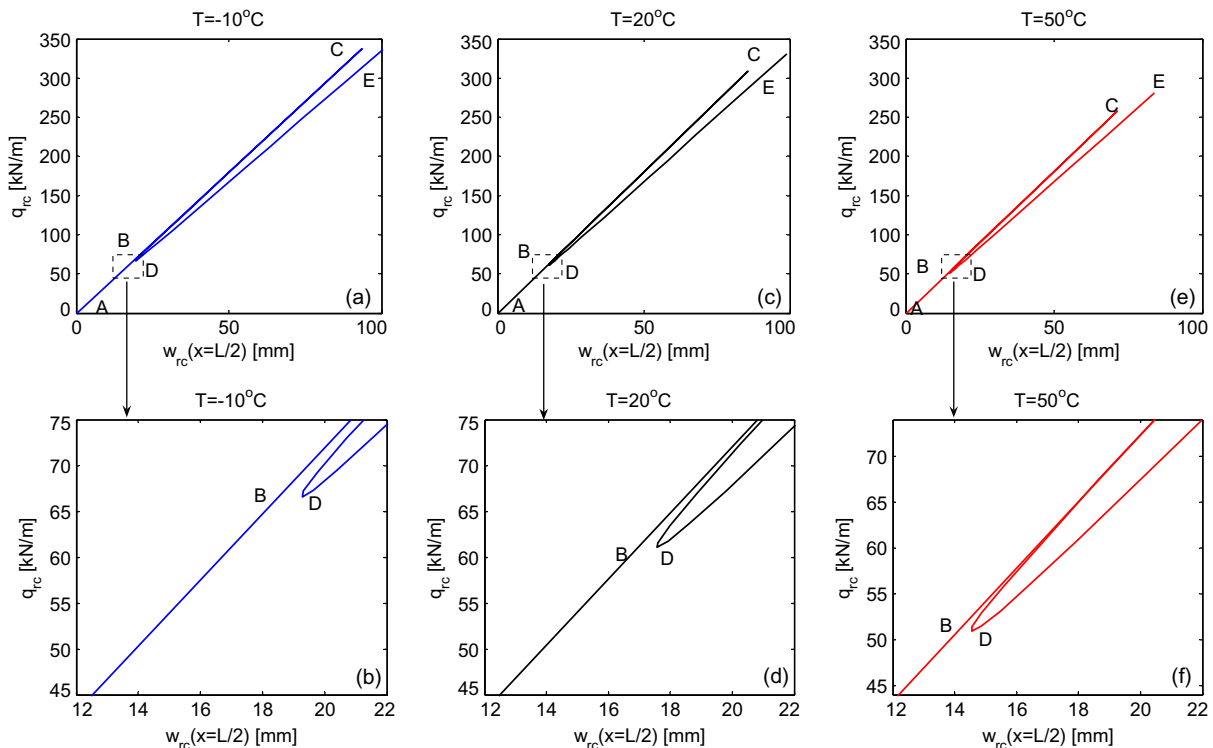

Fig. 7. Equilibrium paths for edge debonding in a simply supported beam under uniform mechanical load and an uniform temperature change: (a) T = −10 °C; (b) T = −10 °C, zoom plot on the snap through point; (c) T = 20 °C; (d) T = 20 °C, zoom plot; (e) T = 50 °C; (f) T = 50 °C, zoom plot.

well within normal thermal conditions. The above aspects and, mainly, the predicted reduction in the debonding strength under normal thermal condition should be taken into account in the design and assessment of the load capacity of the strengthened element.

Acknowledgment

References

ACI Committee 440.2R-02., 2002. Guide for the design and construction of externally bonded FRP systems for strengthening concrete structures american concrete institute. Framington Hills MI.

Au, C., Buyukozturk, O., 2006. Debonding of FRP plated concrete: a tri-layer fracture treatment. Engineering Fracture Mechanics 73 (3), 348–365.

Biel, A., Carlberger, T. 2007. Influence of temperature on cohesive parameters for adhesives. In: Sørensen, BF., Mikelsen, LP., Lilholt, H., Goutianos, S., Abdul-Mahdi, FS. (Eds.), Proceedings of 28th Risø International Symposium on Materials Science.

Blontrock, H. 2003. Analyse en modellering van de brandweerstand van betonelementen uitwendig versterkt met opgelijmde composietlaminaten. Ph.D. thesis, Ghent University, Ghent, Belguim.

Carlberger, T., Biel, A., Stigh, U., 2009. Influence of temperature and strain rate on cohesive properties of a structural epoxy adhesive. International Journal of Fracture 155 (2), 155–166.

Carpinteri, A., 1985. Interpretation of the Griffith instability as a bifurcation of the global equilibrium. In: Shah, S.P. (Ed.), Application of Fracture Mechanics to Cementitious Composites. Martinus Nijhoff Publishers, Dordrecht, pp. 287–316.

Carpinteri, A., Monetto, I., 1999. Snap-back analysis of fracture evolution in multi-cracked solids using boundary element method. International Journal of Fracture 98 (3–4), 225–241.

Carpinteri, A., Cornetti, P., Pugno, N., 2009. Edge debonding in FRP strengthened beams: stress versus energy failure criteria. Engineering Structures 31 (10), 2436–2447.

Dai, J., Ueda, T., Sato, Y., 2005. Development of nonlinear bond-slip model for fiber reinforced plastics sheet – concrete interfaces with a simple method. Journal of Composites for Construction 9 (1), 52–62.

Deng, J., Lee, M.M.K., Moy, S.S.J., 2004. Stress analysis of steel beams reinforced with a bonded CFRP plate. Composites Structures 65 (2), 205–215.

Di Tommaso, A., Neubauer, U., Pantuso, Rostasy, F.S., 2001. Behavior of adhesively bonded concrete-CFRP joints as low and high temperatures. Mechanics of Composite Materials 37 (4), 327–338.

Ferracuti, B., Savoia, M., Mazzotti, C., 2006. A numerical model for FRP-concrete delamination. Composites part B Engineering 37 (4–5), 356–364.

Frostig, Y., 1997. Hygothermal (environmental) effects in high-order bending of sandwich beams with a flexible core and a discontinuous skin. Composite Structures 37 (2), 205–221.

Frostig, Y., Thomsen, O.T., 2007. Buckling and nonlinear response of sandwich panels with a compliant core and temperature-dependent mechanical properties. Journal of Mechanics of Materials and Structures 2 (7), 1355–1380.

Frostig, Y., Thomsen, O.T., 2008a. Thermal buckling and postbuckling of sandwich panels with a transversely flexible core. AIAA Journal 46 (8), 1976–1989.

Frostig, Y., Thomsen, O.T., 2008b. Non-linear thermal response of sandwich panels with a flexible core and temperature dependent mechanical properties. Composites part B Engineering 39 (1), 165–184.

Greco, F., Lonetti, P., Blasi, N., 2007. An analytical investigation of debonding problems in beams strengthened using composite plates. Engineering Fracture Mechanics 74 (3), 346–372.

Hamed, E., Rabinovitch, O., 2007. Geometrically nonlinear effects in the flexural response of masonry walls strengthened with composite materials. Journal of Mechanics of Materials and Structures 2 (5), 829–856.

Karbhari, V.M., Niu, H., Sikorsky, C., 2006. Review and comparison of fracture mechanics based bond strength models for FRP strengthened structures. Journal of Reinforced Plastics and Composites 25 (17), 1757–1794.

Katz, A., Bermal, N., 2000. Modeling the effect of high temperature on the bond of FRP reinforcing bars to concrete. Cement and Concrete Composites 22 (6), 433–443.

Katz, A., Berman, N., Bank, L.C., 1999. Effect of high temperature on the bond strength of FRP rebars. Journal of Composites for Construction 3 (2), 73–81.

Kelmar, E.L., Hordijk, D.A., Hermes, M.C.J., 2008. The influence of temperature on RC beams strengthened with externally bonded CFRP reinforcement. Heron 53 (3), 157–185.

Klamer, E.L. 2006a. The Influence of Temperature on Concrete Structures Strengthened with Externally Bonded CFRP, Report No. O-2006. 04, Eindhoven University of Technology, Department of Architecture, Building and Planning, Structural Design and Construction Technology, Concrete Section.

Klamer, E.L., Hordijk, D.A., Janssen, H.J.M. 2005. The influence of temperature on the debonding of externally bonded. In: CFRP FRPRCS-7 (Fiber Reinforced Plastics for Reinforced Concrete Structures), ACI fall Convention, Kansas City, MO, USA, November 6–9, ACI-SP-230-88, pp. 1551–1570.

Klamer, E.L., Hordijk, D.A., Kleinman, C.S. 2006b. Debonding of CFRP laminates externally bonded to concrete specimens at low and high temperatures. Third International Conference on FRP Composites in Civil Engineering (CICE 2006), December 13–15, Miami, Florida, USA.

Lei, Y., 2005. J-integral evaluation for cases involving non-proportional stressing. Engineering Fracture Mechanics 72 (4), 577–596.

Lovinger, Z. 2002. Bonded Tile Wall Systems – Failure Criteria and a Two Dimensional (2D) Analysis, M.Sc. Thesis, Faculty of Civil and Environmental Engineering, Technion – Israel Institute of Technology.

Lovinger, Z., Frostig, Y., 2004. High order behavior of sandwich plates with free edges-edge effects. International Journal of Solids and Structures 41 (3–4), 979–1004.

Lu, X.Z., Teng, J.G., Ye, L.P., Jiang, J.J., 2005a. Bond-slip models for FRP sheets/plates bonded to concrete. Engineering Structures 27 (6), 920–937.

Lu, X.Z., Ye, L.P., Teng, J.G., Jiang, J.J., 2005b. Meso-scale finite element model for FRP sheets/plates bonded to concrete. Engineering Structures 27 (4), 564–575.

Nairn, J.A., 2000. Exact and variational theorems for fracture mechanics of composites with residual stresses, traction-loaded cracks, and imperfect interfaces. International Journal of Fracture 105 (3), 243–271.

Niu, H., Wu, Z., 2005. Numerical analysis of debonding mechanism in FRP-strengthened RC beams. Computer-aided Civil and Infrastructure Engineering 20 (5), 354–368.

Qiao, P., Xu, Y., 2005. Thermal effects on the fracture of adhesively bonded composite concrete interface. Journal of Advanced Materials 37 (2), 56–62.

Rabinovitch, O., 2004. Fracture-mechanics failure criteria for RC beams strengthened with FRP strips – a simplified approach. Composites Structures 64 (3–4), 479–492.

Rabinovitch, O. 2007a. On thermal stresses in RC beams strengthened with externally bonded FRB strips. In: FRPRCS-8 (Fiber Reinforced Plastics for Reinforced Concrete Structures), Patras, Greece, July 16–18, 2007.

Rabinovitch, O., 2007b. Piezoelectric control of edge debonding in beams strengthened with composite materials – part I: analytical modeling. Journal of Composite Materials 41 (5), 525–546.

Rabinovitch, O., 2007c. Piezoelectric control of edge debonding in beams strengthened with composite materials – Part II: failure criteria and optimization. Journal of Composite Materials 41 (6), 657–677.

Rabinovitch, O., 2008a. Debonding analysis of fiber reinforced polymer strengthened beams: cohesive zone modeling versus a linear elastic fracture mechanics approach. Engineering Fracture Mechanics 75 (10), 2842–2859.

Rabinovitch, O., 2008b. Cohesive interface modeling of debonding failure in FRP strengthened beams. ASCE Journal of Engineering Mechanics 134 (7), 578–788.

Rabinovitch, O., Frostig, Y., 2000. Closed-form high-order analysis of RC beams strengthened with FRP strips. Journal of Composites for Construction 4 (2), 65–74.

Rabinovitch, O., Frostig, Y., 2001. Delamination failure of RC beams strengthened with FRP strips – a closed-form high-order and fracture mechanics approach. Journal of Engineering Mechanics, ASCE 127 (8), 852–861.

Rabinovitch, O., Frostig, Y., 2003. Experiments and analytical comparison of RC beams strengthened with externally bonded CFRP strips. Composites part B Engineering 34 (8), 663–667.

Rabinovitch, O., Frostig, Y., 2006. Fracture mechanics approach to geometrically nonlinear debonding problems in RC beams strengthened with composite materials. Advances in Structural Engineering 9 (6), 765–777.

Rice, J.R., 1968. A path independent integral and the approximated analysis of strain concentration by notches and cracks. Journal of Applied Mechanics, Transaction of the ASME 35 (6), 379–386.

Roberts, T.M., Haji-Kazemi, H., 1989. Theoretical study of the behavior of RC beams strengthened by externally bonded steel plates. Proceeding of the Institution of Civil Engineering 87 (2), 39–55.

Saafi, M., 2002. Effect of fire on FRP reinforced concrete members. Composite Structures 58 (1), 11–20.

Stratford, T., Cadei, J., 2006. Elastic analysis of adhesion stresses for the design of a strengthening plate bonded to a beam. Construction and Building Materials 20 (1–2), 34–45.

Taljsten, B., 1996. Strengthening of concrete prism using the plate-bonding technique. International Journal of Fracture 82 (3), 253–266.

Teng, J.G., Yuan, H., Chen, J.F., 2006. FRP-to-concrete interfaces between two adjacent cracks: theoretical model for debonding failure. International Journal of Solids and Structures 43 (18–19), 5750–5778.

Tschegg, E.K., Krassnitzer, T., 2008. Mode I fracturing properties of epoxy bonding paste. International Journal of Adhesion and Adhesives 28 (7), 340–349.

Wang, J., 2006a. Cohesive zone model of intermediate crack induced debonding of FRP-plated reinforced concrete beam. International Journal of Solids and Structures 43 (21), 6630–6648.

Wang, J., 2006b. Debonding of FRP plated reinforced concrete beam, a bond-slip analysis. I. theoretical formulation. International Journal of Solids and Structures 43 (21), 6649–6664.

Wilson, W.K., Yu, I.W., 1979. The use of the J-integral in thermal stress crack problems. International Journal of Fracture 15 (4), 377–387.

Wu, Z., Yin, J., 2003. Fracturing behaviors of FRP strengthened concrete structures. Engineering Fracture Mechanics 70 (10), 1339–1355.

Yang, Q.S., Peng, X.R., Kwan, A.K.H., 2006. Strain energy release rate for interfacial cracks in hybrid beams. Mechanics Research Communications 33 (6), 796–803.

Yuan, H., Teng, J.G., Seracino, R., Wu, Z.S., Yao, J., 2004. Full-range behavior of FRP to concrete bonded joints. Engineering Structures 26 (5), 553–565.